The Role of Cation Acidity on the Competition between Hydrogen Evolution and CO2 Reduction on Gold Electrodes

The role of cation acidity on the competition between hydrogen evolution and CO_2 reduction on gold electrodes

Mariana C. O. Monteiro[a], Federico Dattila[b], Núria López[b], Marc T. M. Koper[a,*]

[a]Leiden Institute of Chemistry, Leiden University, P.O. Box 9502, 2300 RA Leiden, The Netherlands

[b]Institute of Chemical Research of Catalonia (ICIQ), The Barcelona Institute of Science and Technology (BIST), Av. Països Catalans 16, 43007 Tarragona, Spain.

Supporting Information

Gold electrode characterization

Scanning Electron Microscopy (SEM) and Energy Dispersive X-Ray Spectroscopy (EDX) of the gold electrode used in this study.

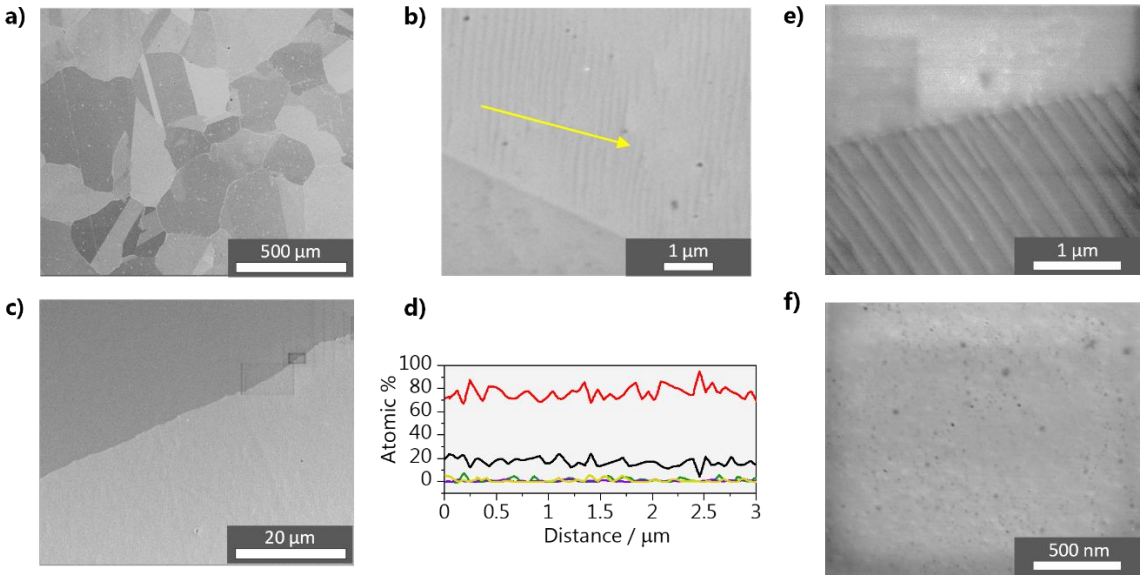

Figure S1. a)-c) SEM micrographs and d) EDX line spectra of the gold electrode (region marked with a yellow arrow) used for the experiments after polishing with diamond suspension and flame annealing. The lines refer to the following signals: --- (black) C K, --- (green) O K, --- (purple) Al K and --- (red) Au M. e) and f) show SEM micrographs of the same polycrystalline gold electrode after hydrogen evolution in 0.1 M Li_2SO_4 + 1 mM Nd^{3+} (experiment from Figure S7a).

Potential opening experiments at pH 3 (0.1 M M_2SO_4)

Blank voltammetry of the gold electrode before the experiments performed at pH 3 in 0.1 M M_2SO_4 electrolytes with M^{n+} = Li^+, Na^+, K^+ and Cs^+. The overlapping voltammograms assure the stability of the gold electrode throughout the measurements.

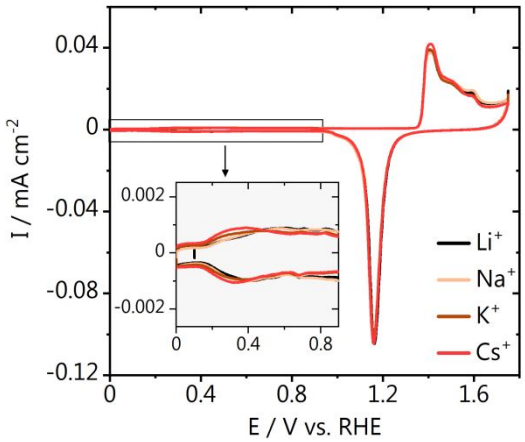

Figure S2. Blank voltammetry of the gold electrode after flame annealing taken at 50 mV s^{-1} in 0.1 H_2SO_4.

Consecutive cathodic/anodic voltammetry of the gold electrode in CO_2 atmosphere (pH 3, 0.1 M M_2SO_4 electrolytes with M^{n+} = Li^+, Na^+, K^+ and Cs^+) going to different negative potentials.

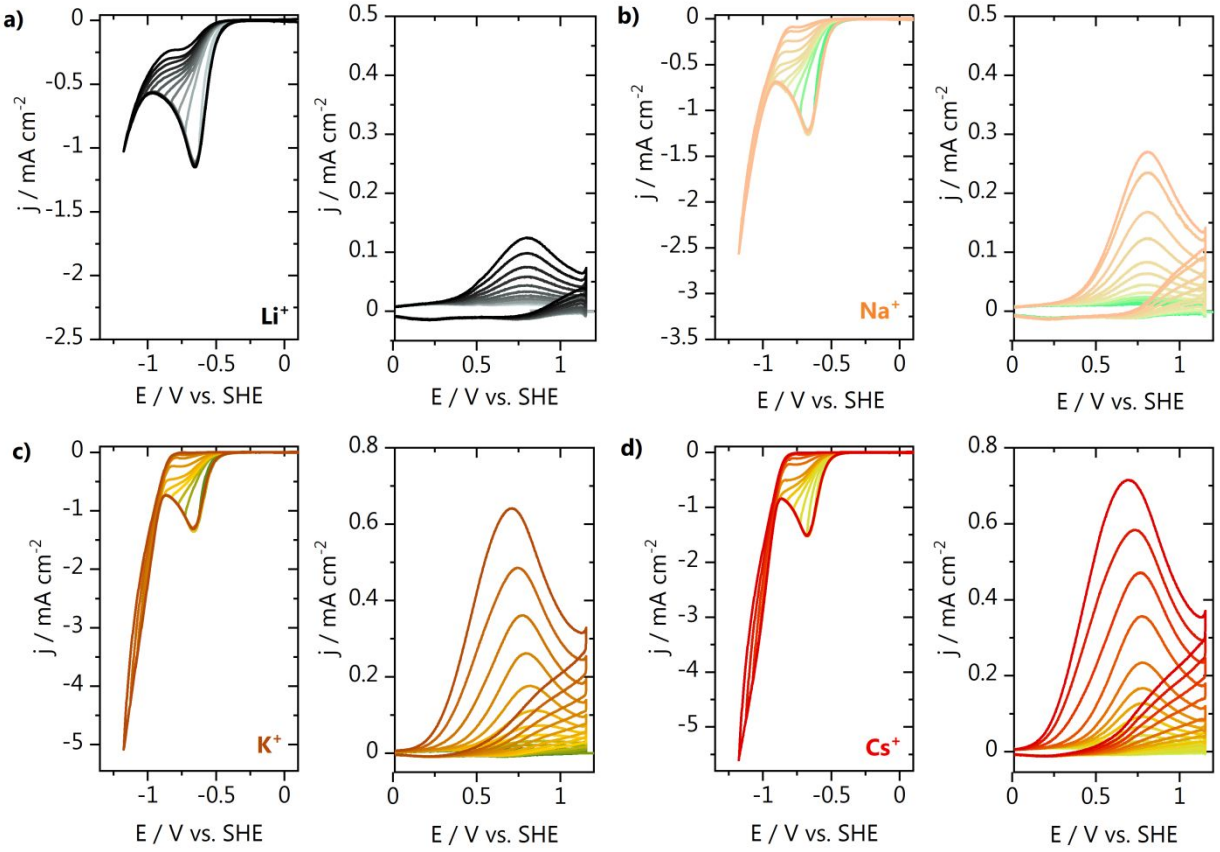

Figure S3. a)-d) Consecutive cathodic/anodic voltammetry of the CO_2 reduction potential opening experiments in 0.1 M M_2SO_4 with M^{n+} = Li^+, Na^+, K^+, Cs^+ at pH = 3.

HER and CO_2RR experiments at pH 6.8 (0.1 M *M*HCO_3)

Blank voltammetry of the gold electrode taken before the experiments performed at pH 6.8 in 0.1 M $MHCO_3$ electrolytes with M^{n+} = Li^+, Na^+, K^+ and Cs^+.

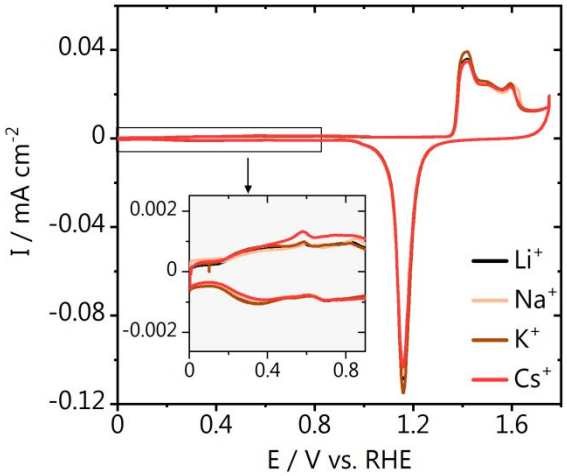

Figure S4. Blank voltammetry of the gold electrode after flame annealing taken at 50 mV s^{-1} in 0.1 H_2SO_4.

Similarly to our experiments in acidic media, in bicarbonate the CO produced in the cathodic scan can also be detected in the positive-going scan. The inset of Figure S5b, shows the CO produced after the gold electrode is polarized negatively and that the highest amount of CO is produced in the Cs^+ and K^+ electrolytes. The two peaks observed in the CO oxidation voltammetry in bicarbonate are due to diffusion limitation by two different species, namely, CO and OH^-, as a function of the local pH. In our previous work, we find that between pH 7 and 11, CO oxidation by water and OH^- gives rise to the first and second peak observed in the voltammetry, respectively, and that the current of the second peak is diffusion limited by the OH^- concentration, since it is lower than the CO concentration at this pH.[1]

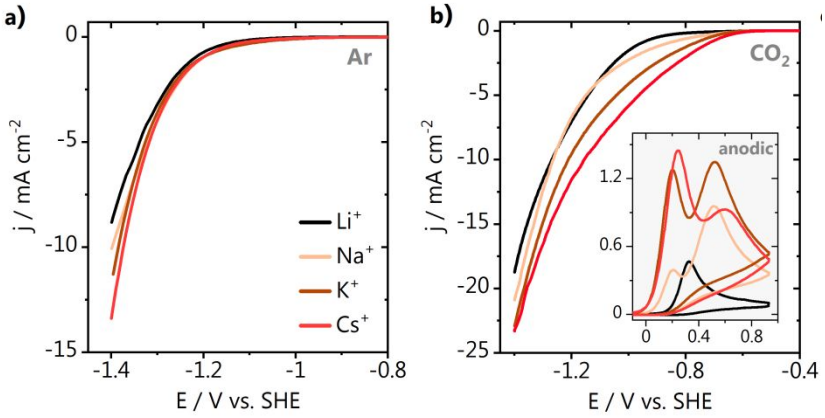

Figure S5. Cyclic voltammetry of a) water reduction and b) CO_2 reduction in 0.1 M $MHCO_3$, pH 9 (argon atmosphere) and pH 7 (CO_2 atmosphere).

Hydrogen evolution in electrolytes containing multivalent cations

The blank voltammetry of the gold electrode before the experiments performed at pH 3 in 0.1 M Li_2SO_4 + 1 mM M^{n+} electrolytes with M^{n+} = Li^+, Cs^+, Be^{2+}, Mg^{2+} , Al^{3+} , Nd^{3+} , Ce^{3+} and 0.2 M $LiClO_4$ + 2 mM M^{n+} with M = Ca^{2+}, Ba^{2+} is shown in Figure S6a. Figure S6b shows an example of the gold electrode blank voltammetry before and after the hydrogen evolution measurements, which indicates the cleanliness, lack of changes in electrochemical surface area and stability of the electrode surface during experiments (of course, in regards to what can be detected by blank voltammetry). Owing to the short term of the experiments, and with the information from the example control SEM images shown in Figure S1e and Figure S1f, we do not expect that there is any significant nanoparticle deposition from the gold counter onto our working electrode affecting the electrocatalysis.

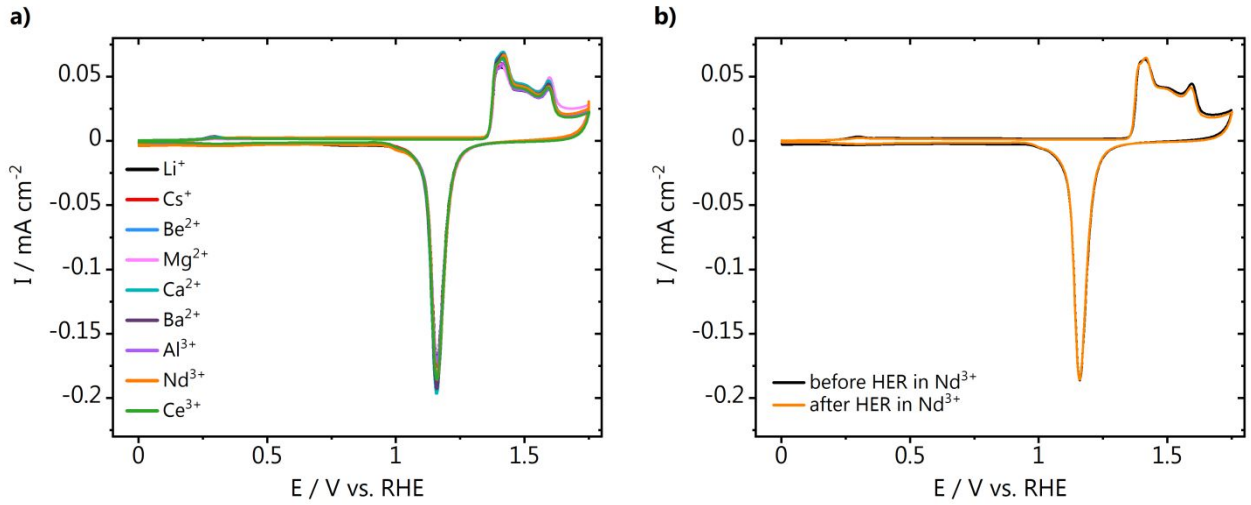

Figure S6. Blank voltammetry of the gold electrode a) after flame annealing, before the HER experiments performed in the presence of the different cations and b) before and after HER in Nd^{3+}. Blank CVs were taken at 50 mV s^{-1} in 0.1 H_2SO_4.

CVs of the gold electrode during hydrogen evolution performed at pH 3 in 0.1 M Li_2SO_4 + 1 mM M^{n+} electrolytes with M^{n+} = Li^+, Cs^+, Be^{2+}, Mg^{2+}, Al^{3+}, Nd^{3+}, Ce^{3+} and 0.2 M $LiClO_4$ + 2 mM M^{n+} with M^{n+} = Ca^{2+}, Ba^{2+}. All electrolytes were saturated with Argon prior to the measurements.

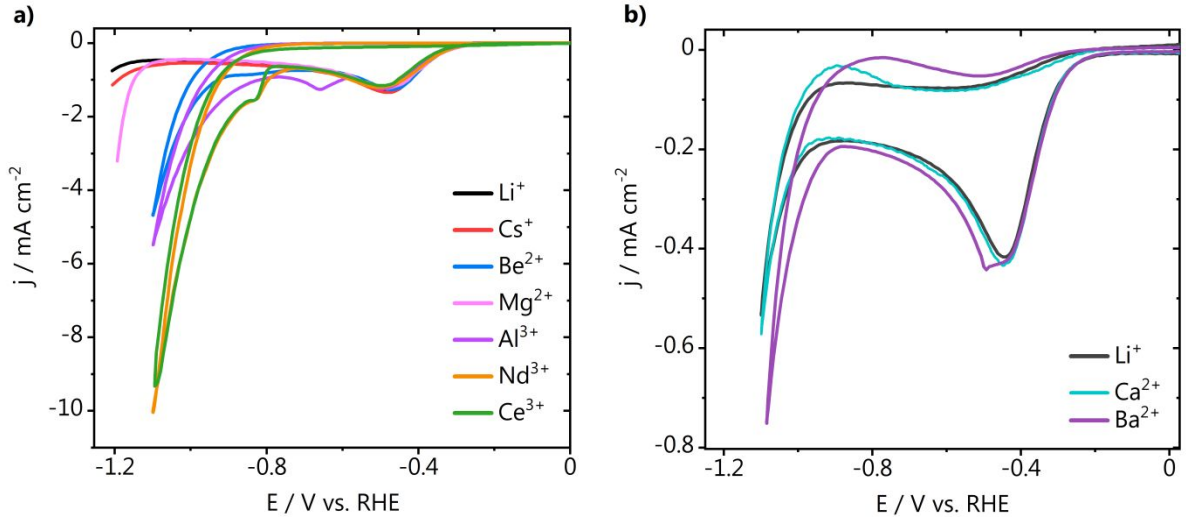

Figure S7. Cyclic voltammetry of HER in a) 0.1 M Li_2SO_4 or b) 0.1 M $LiClO_4$ electrolyte solutions containing different cations.

Relationship between cation acidity and Gibbs free energy of hydration.[2]

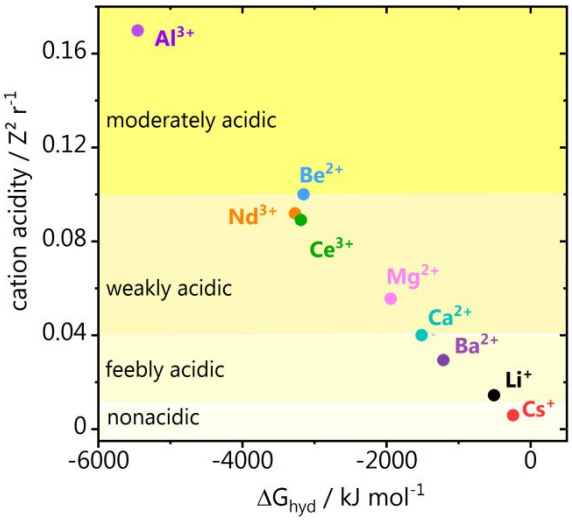

Figure S8. Cation acidity and Gibbs free energy of hydration for the different multivalent cations used in this work.

Cyclic voltammetry of HER showing the effect of cation hydrolysis on the first and second regimes of proton reduction and on hydroxide deposition.

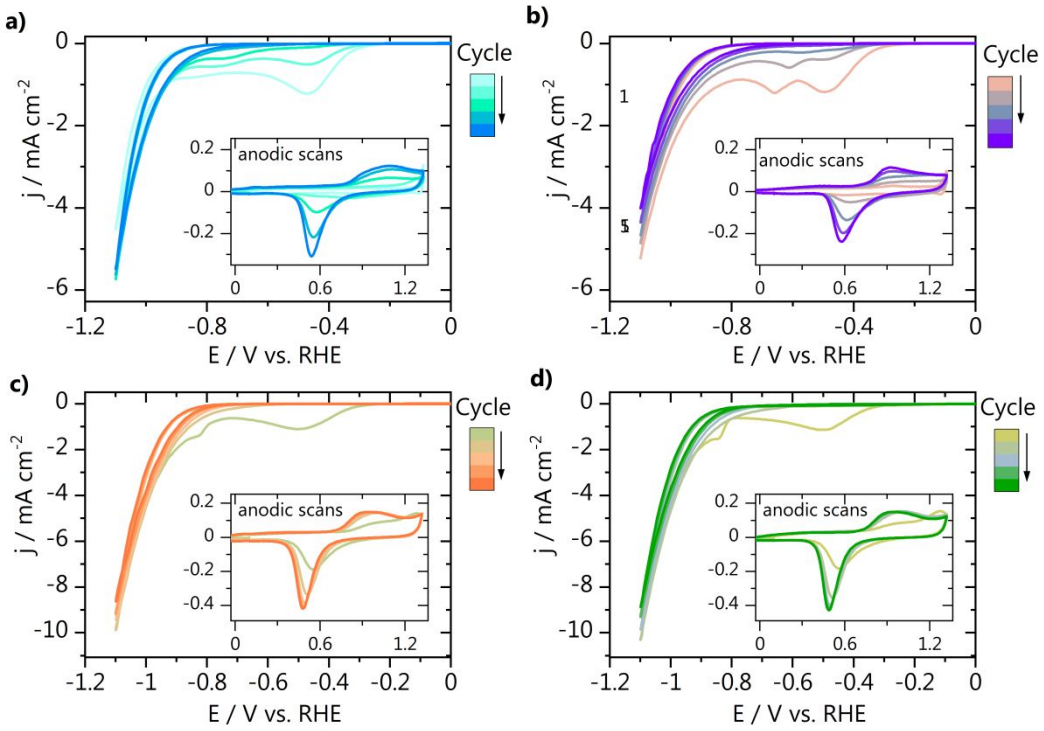

Figure S9. Hydrogen evolution cyclic voltammetry performed at pH 3 in 0.1 M Li_2SO_4 + 1 mM M^{n+} electrolytes with M^{n+} being a) Be^{2+}, b) Al^{3+}, c) Nd^{3+}, d) Ce^{3+}. An anodic scan recorded directly after HER is shown in the graph inset.

Density functional theory modeling

We carried out density functional theory (DFT) simulations through the Vienna Ab Initio Package(VASP).[3,4] We chose the PBE density functional[5] including dispersion through the DFT-D2 method,[6,7] with our reparametrized C_6 coefficients.[8] Inner electrons were represented by PAW pseudopotentials[9,10] and the monoelectronic states for the valence electrons were expanded as plane waves with a kinetic energy cutoff of 450 eV. Since Nd presents a localized *f* electron, which leads to self-interaction error, we applied a Hubbard correction U_{eff} = 6.76 eV – 0.76 eV to the Nd atom following the Dudarev's approach.[11] This value was taken from a previous computational work, where the authors assessed electronic and magnetic properties for a Nd adatom.[12]

We modeled the experimental system as in our recent work.[13] We employed a 3√3×3√3–*R*30° Au(111) supercell, which included 4 layers with 15.3 Å × 15.3 Å lateral dimensions and overall thickness 30.0 Å (8 Å vacuum). The solvation layer accounted for 72 H_2O molecules within 15 Å and it was retrieved from our work mentioned above.[13] During that study,[13,14] the system was optimized for more than 10 ps via AIMD simulation in a canonical NVT ensemble at 300 K regulated by a Nosé-Hoover thermostat.[13,15–17]. We introduced two cations M^{n+} (Li^+, Cs^+, Mg^{2+}, Ba^{2+}, Al^{3+}, Nd^{3+}) within the first solvation layer, whilst we removed 2*n* hydrogens from water molecules in the fourth water bilayer to keep charge balance (*n* = cation charge). Considering the thickness of the solvation layer (1.4 nm), the geometrical area (2.0 nm^2) and the overall number of solvent molecules (72), a cation surface coverage of 0.08 ML (2/27) is equivalent to a surface concentration between 1.0 (2/N_A mol within a volume of 3.29 nm^3) and 1.6 M (2/72 of water

molar concentration, 55.5 M). Besides, to better mimic explicit electrostatic effects, we applied an electric field of –0.3 V Å^{-1},[8,18] equivalent to a potential of –0.9 V vs. potential of zero charge (U_{PZC}), assuming an electrical double layer thickness of 3 Å.[19,20] Since the U_{PZC} for polycrystalline gold is reported as +0.2 V vs SHE,[21] the applied electric field is equivalent to an electric potential of –0.7 V vs. SHE, Supporting Equation 1.

$$U\ (\text{vs. SHE}) = U_{\text{PZC}} + \vec{E}_{\text{EDL}} \cdot d_{\text{EDL}} \quad (1)$$

The Au/water/cation systems underwent 2 ps of AIMD simulations. Finally, we added either a CO_2 or an additional water molecule (0.04 ML, 1/27) to the equilibrated Au/water and Au/water/cations model, which adsorbed on the surface close to one of the cations. Besides, to check a reference case with proton as the cation, we replaced the 2 optimized Li^+ atoms in the Au/H_2O/Li^+ systems with H^+. The resulting 6 Au/water/M^{n+}/*ads* and 1 Au/water/H^+/*ads* systems (*ads* = *CO_2, *H_2O) were further optimized for 2 ps to assess the activation of CO_2 and H_2O in the presence and absence of a metal cation. Since cations, adsorbates CO_2, and the explicit solvation later were placed only on one side of the slab, we applied an additional dipole correction to remove spurious contributions arising from the asymmetric slab model.[22]

Cation-water radial distribution functions

We obtained the cation-water radial distribution functions, $g_{M^{n+}\text{-}H2O}(r)$ from the 2 ps equilibration of the Au/water/M^{n+} systems to estimate the density of water molecules around the two M^{n+} centers introduced in the supercell. First, we calculated the distribution of distances of H_2O oxygens from the cation, $\eta(r)$, defined for all the molecular dynamics steps within an interval (r, $r + \Delta r$), where r is the position vector from M^{n+} and Δr is its differential. We then normalized $\eta(r)$ for the surface density of cations ρ corresponding to 2D annulus formed by the solvation layer, Supporting Equation 2.

$$g(r)_{\text{2D}} = \frac{\eta(r)}{2\pi r \cdot \Delta r \cdot \rho} \quad (2)$$

In Supporting Equation 3, $g(r)$ is the radial distribution function (dimensionless), $\eta(r)$ the distribution of distances (dimensionless), r the module of the position vector, Δr its differential (both in Å), and ρ the cation surface density (Å^{-2}). Cation-water radial distribution functions are reported in Supporting Figure 10 and the parameters of the Lorentzian fit on the first solvation shell peaks are shown in Supporting Table 1. A Lorentzian fit was applied through Supporting Equation 3, as in Ref. 13.

$$g(r) = g(r)_0 + \left(\frac{2A}{\pi}\right) \cdot \left(\frac{w}{4(r - d_{M-0})^2 + w^2}\right) \quad (3)$$

$g(r)$ is the radial distribution function, r the position vector (Å), w the full width at half maximum (Å), $d_{M+\text{-}O}$ the cation-oxygen bond length (Å), whilst $g(r)_0$ (dimensionless) and A (Å) are fit parameters. The parameters of the Lorentzian fit and the resulting estimation of the cation-oxygen distances in the first solvation shell are reported in Supporting Table 1 and agree with previous experimental and theoretical reports.[23,24] The cation-oxygen bond length ($d_{M\text{-}O}$) and its associated uncertainty are obtained from the fit parameters on the $g(r)$ first peaks. The term $d_{M\text{-}O(S.A.)}$ stands for averages of state-of-the-art values for cation-water distances.[23,24]

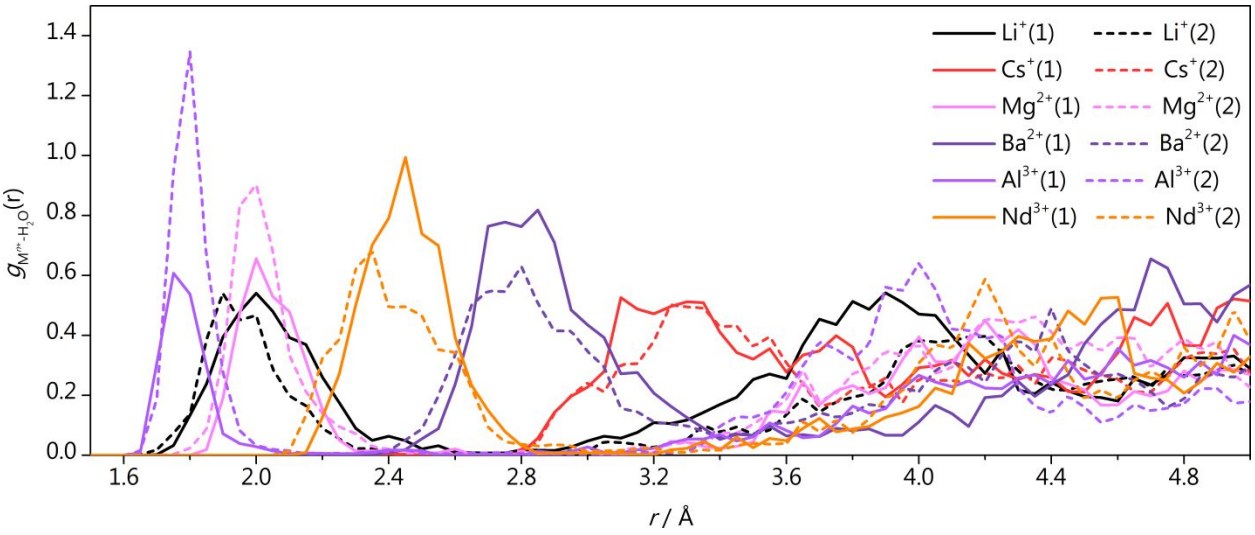

Figure S10. Cation solvation shells during 2 ps equilibration (0-2 ps) of the Au/water/M^{n+}, described by the cation-water radial distribution functions.

Supporting Table 1. Parameters of the Lorentzian fit and distances between cation and water molecules in the first solvation shell, estimated from the position of the first peak of cation-water radial distribution functions, Supporting Figure 10, for an AIMD equilibration of 2 ps. $g(r)_0$, *A, w* (Å) and χ^2_v are fit parameters. Uncertainty associated with fit parameters is given as standard deviation of the data, whilst uncertainty related to averages of state-of-the-art values for cation-water distances, $d_{M\text{-}O(S.A.)}$, is taken from Ref.[23,24].

M^{n+}	$g(r)_0$	*A* / Å	*w* / Å	χ^2_v	$d_{M\text{-}O}$ / Å	$d_{M\text{-}O(S.A.)}$ / Å
$Li^+(1)$	–0.030 ± 0.009	0.281 ± 0.018	0.31 ± 0.02	1.1E–03	2.021 ± 0.006	2.08 ± 0.07
$Li^+(2)$	–0.022 ± 0.008	0.206 ± 0.013	0.233 ± 0.018	1.1E–03	1.945 ± 0.005	
$Cs^+(1)$	–0.09 ± 0.02	0.35 ± 0.05	0.48 ± 0.07	3.5E–03	3.275 ± 0.017	3.14 ± 0.08
$Cs^+(2)$	–0.057 ± 0.013	0.34 ± 0.04	0.46 ± 0.05	2.7E–03	3.326 ± 0.015	
$Mg^{2+}(1)$	–0.031 ± 0.012	0.214 ± 0.017	0.196 ± 0.018	2.1E–03	2.028 ± 0.005	2.09 ± 0.04
$Mg^{2+}(2)$	–0.023 ± 0.011	0.241 ± 0.013	0.154 ± 0.010	2.0E–03	1.996 ± 0.003	
$Ba^{2+}(1)$	–0.028 ± 0.013	0.49 ± 0.03	0.36 ± 0.03	3.6E–03	2.826 ± 0.007	2.81
$Ba^{2+}(2)$	–0.025 ± 0.010	0.40 ± 0.02	0.40 ± 0.03	1.8E–03	2.798 ± 0.008	
$Al^{3+}(1)$	–0.012 ± 0.007	0.124 ± 0.008	0.110 ± 0.10	9.6E–04	1.772 ± 0.002	1.887 ± 0.015
$Al^{3+}(2)$	–0.026 ± 0.011	0.232 ± 0.011	0.102 ± 0.006	2.4E–03	1.791 ± 0.002	
$Nd^{3+}(1)$	–0.042 ± 0.011	0.41 ± 0.02	0.259 ± 0.015	2.4E–03	2.445 ± 0.004	2.472 ± 0.033
$Nd^{3+}(2)$	–0.039 ± 0.015	0.37± 0.03	0.34 ± 0.03	3.1E–03	2.384 ± 0.009	

Cation coordination number

To obtain the coordination number $N_{M\text{-}O}$ of the multivalent cations M^{n+}, we assigned a bond value equal to one if the cation-oxygen distance $r_{M\text{-}O}$ was equal or lower than the cation-oxygen bond length $d_{M\text{-}O}$, Supporting Table 1. Otherwise, the bond value was set to zero if $r_{M\text{-}O}$ was larger than a certain threshold $th_{M\text{-}O}$: 2.5, 3.5, 2.4, 3.5, 2.0, 2.8 Å for Li^+, Cs^+, Mg^{2+}, Ba^{2+}, Al^{3+}, Nd^{3+} respectively (Supporting Figure 10). Between these extremes, $N_{M\text{-}O}$ was calculated through Supporting Equation 4 following a decay controlled by the error function (erf), Supporting Equation 4.[25] In Supporting Equation 4, $N_{M\text{-}O}$ is the cation coordination number (dimensionless), $r_{M\text{-}O}$ is the cation-oxygen distance (Å), $d_{M\text{-}O}$ the cation-oxygen bond length (Å), $th_{M\text{-}O}$ the cation-oxygen threshold (Å) and avg stands for average. In Supporting Equation 5, *t (*dimensionless*)* is the variable of integration and 0 and *z* represent the integration limits.

$$N_{M-O} = \frac{1}{2} - \frac{1}{2}\mathrm{erf}\left(\frac{r_{M-O} - \mathrm{avg}(d_{M-O}, th_{M-O})}{0.2\ \text{Å}}\right) \quad (4)$$

$$\mathrm{erf}\,(z) = \frac{2}{\sqrt{\pi}}\int_0^z \exp\left(-t^2\right)dt \quad (5)$$

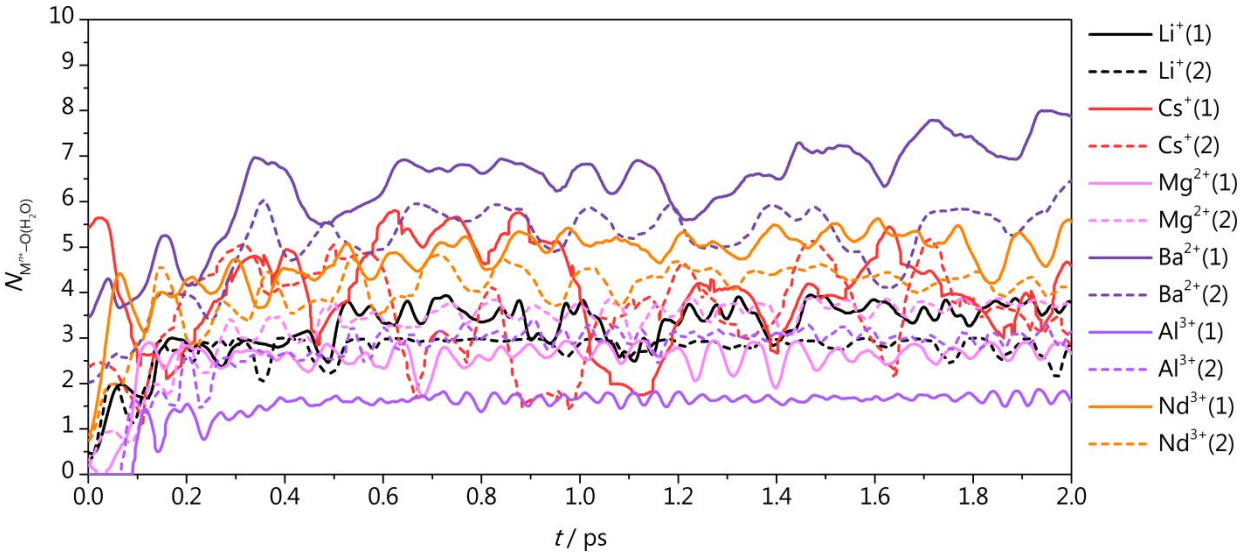

Figure S11. Cation coordination numbers to oxygen atoms in water ($N_{M\text{-}O(H2O)}$) during equilibration of the Au/water/M^{n+} system (from 0 to 2 ps).

Supporting Table 2. Cation coordination numbers to oxygen atoms in water ($N_{M\text{-}O(H2O)}$) as calculated through Supporting Equation 4 for Au/water/M^{n+} during 2 ps AIMD at 300 K (Figures S11). Coordination numbers are reported as averages with their associated standard deviation $\sigma(N_{M\text{-}O})$, median, maximum, and minimum values.

	$N_{M\text{-}O(H2O)}$ (Au/water/M^{n+})			
M^{n+}	Mean	Median	Max	Min
$Li^+(1)$	3.5 ± 0.3	3.6	3.9	2.5
$Li^+(2)$	2.8 ± 0.2	2.9	3.0	2.1
$Cs^+(1)$	3.7 ± 0.9	3.9	5.4	1.7
$Cs^+(2)$	3.7 ± 0.7	3.7	5.2	2.0
$Mg^{2+}(1)$	2.6 ± 0.2	2.7	2.9	1.9
$Mg^{2+}(2)$	3.6 ± 0.2	3.7	3.9	3.0
$Ba^{2+}(1)$	6.9 ± 0.6	6.9	8.0	5.6
$Ba^{2+}(2)$	5.4 ± 0.5	5.6	6.5	4.1
$Al^{3+}(1)$	1.68 ± 0.08	1.7	1.9	1.5
$Al^{3+}(2)$	3.03 ± 0.14	3.1	3.3	2.4
$Nd^{3+}(1)$	5.1 ± 0.3	5.1	5.6	4.2
$Nd^{3+}(2)$	4.3 ± 0.2	4.3	4.7	3.7

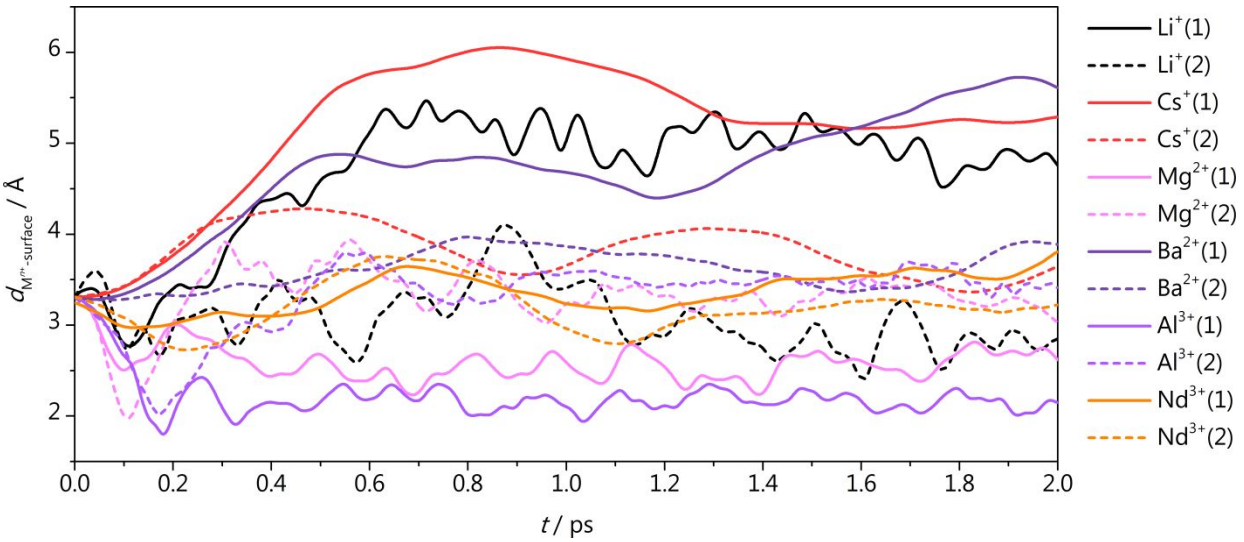

Figure S12. Distance between cation (M^{n+}) and surface calculated during equilibration of the Au/water/M^{n+} system (from 2 to 4 ps).

Cation accumulation at the Outer Helmholtz layer

To assess the thermodynamics of cation accumulation at outer Helmholtz plan (OHP), we applied the methodology introduced by Resasco *et al.*[26] The energy of a solvated cation at the bulk electrolyte can be referenced to the energy of the bulk metal following the principles of the Computational Hydrogen Electrode.[27] In the following lines, we define such methodology for the case of alkali cations, which can be easily generalized to multivalent species. At the standard reduction potential U_0,[28] a cation M^+ is in equilibrium with its reduced state M, Supporting Equation 6. Thus, we can derive the energy of the cation/electron pair at a given potential U vs SHE from the DFT energy of the bulk alkali metal, Supporting Equation 7.

$$\mathrm{M}^+ + \mathrm{e}^- \leftrightarrow \mathrm{M},\ U = U_0 \tag{6}$$

$$E_{\mathrm{M}^+ + \mathrm{e}^-} = E_{\mathrm{M}} - |\mathrm{e}^-|\,(U - U_0) \tag{7}$$

We can instead estimate the energy of a cation at the OHP at U = 0 V vs SHE from our *ab initio* molecular dynamics simulations, since we specifically inserted two metals at the OHP, which donate their valence electron to the solvation layer, Supporting Equation 8. * accounts for the gold surface and the label env for the environment, i.e. the solvation layer and the second cation. Thus, we can calculate the thermodynamic driving force for one of the two cations to accumulate at the OHP as in Supporting Equation 9 for 50 AIMD snapshots after 1 ps equilibration (every 20 fs from 1 ps to 2 ps).

$$* + \mathrm{env} + \mathrm{M} \rightarrow * + \mathrm{env} + \mathrm{M}^+ + \mathrm{e}^-, E_{\mathrm{M}^+ + \mathrm{e}^-}(\mathrm{OHP}) \tag{8}$$

$$\Delta E = E_{\mathrm{M}^+ + \mathrm{e}^-}(\mathrm{OHP}) - E_{\mathrm{M}^+ + \mathrm{e}^-}(\mathrm{bulk}) \tag{9}$$

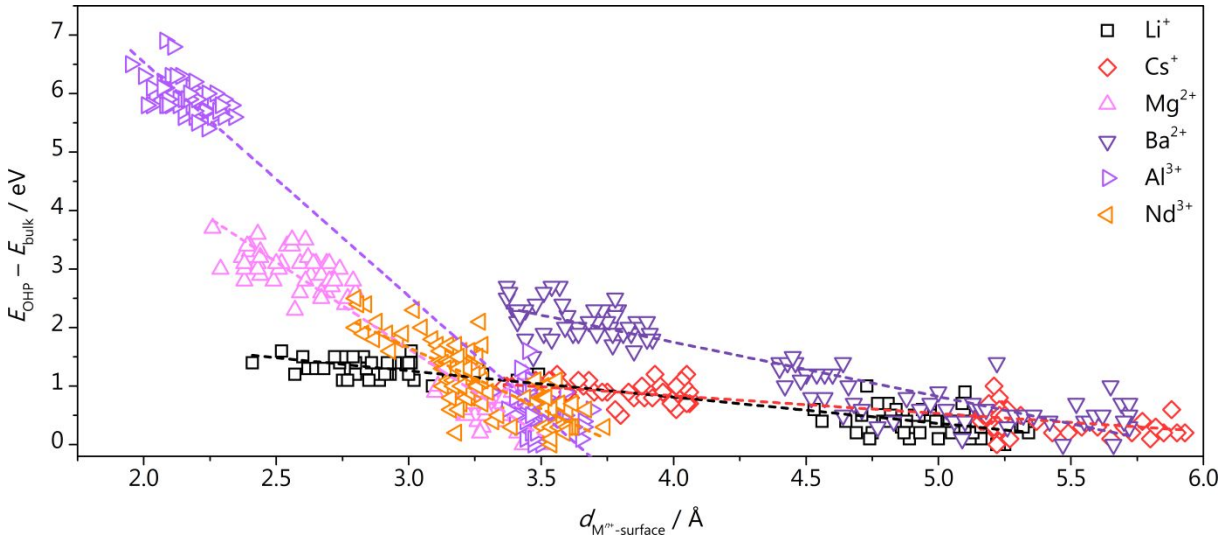

Figure S13. Correlation between the thermodynamic driving force for cation accumulation at the OHP estimated at U = 0 V versus SHE and cation-surface distance. The data points have been referenced to the minimum for each cation, respectively –2.4, –2.2, –6.7, –8.1, –11.4, –8.5 eV for Li^+, Cs^+, Mg^{2+}, Ba^{2+}, Al^{3+}, and Nd^{3+}. All the data points are therefore negative, confirming that cation accumulation at the OHP is an exothermic process.

Supporting Table 3. Fit parameters for linear correlations shown in Figure S13: $E_{\mathrm{OHP}} - E_{\mathrm{bulk}} = a + b * d_{\mathrm{M}^{n+}-\mathrm{surface}}$

M^{n+}	a / eV	b / eV Å^{-1}	R^2
Li^+	+2.61 ± 0.07	–0.45 ± 0.02	0.87
Cs^+	+2.05 ± 0.09	–0.30 ± 0.02	0.70
Mg^{2+}	+10.5 ± 0.3	–2.97 ± 0.08	0.93
Ba^{2+}	+5.5 ± 0.2	–0.93 ± 0.04	0.84
Al^{3+}	+14.5 ± 0.2	–4.00 ± 0.06	0.98
Nd^{3+}	+8.0 ± 0.5	–2.1 ± 0.2	0.65

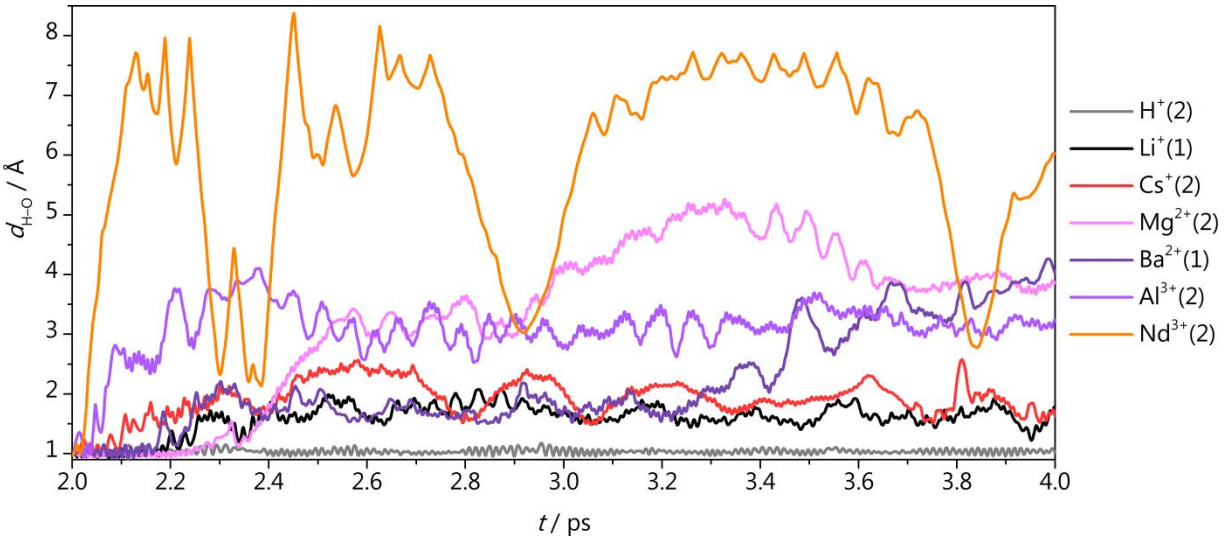

Figure S14. H-O Distances in the adsorbed water molecule for the Au/water/M^{n+}/*H_2O system (from 2 to 4 ps). For all the metal cations *H_2O dissociates into OH^- and H^+ after less than 0.3 ps.

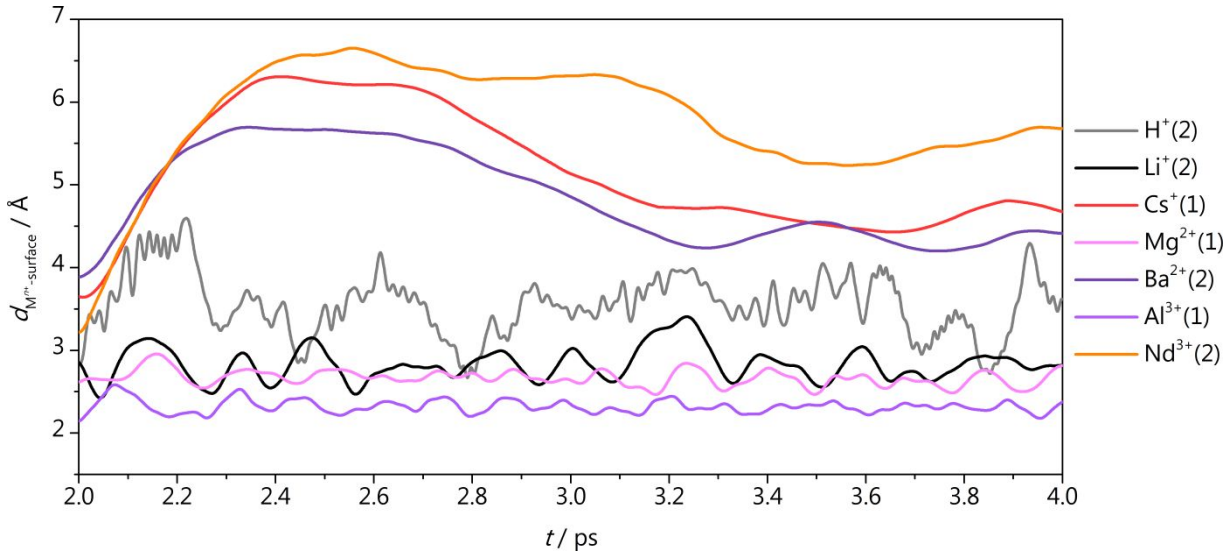

Figure S15. Distance between cation (M^{n+}) and surface calculated for the Au/water/M^{n+}/*H_2O system (from 2 to 4 ps).

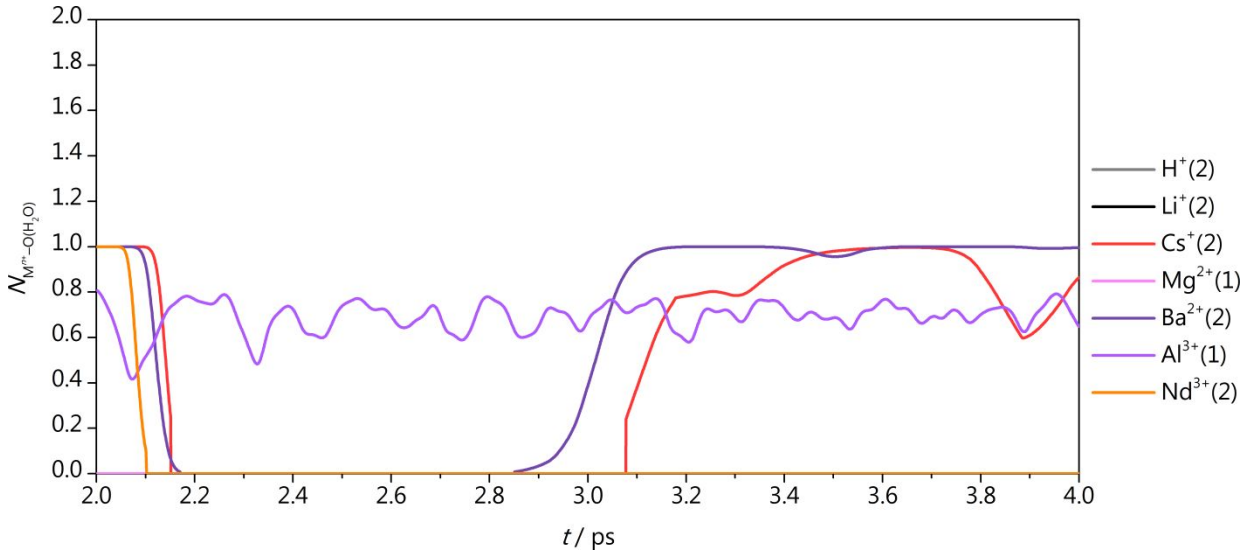

Figure S16. Cation coordination numbers to oxygen atoms in adsorbed H_2O ($N_{M\text{-}O(H2O)}$) for the Au/water/M^{n+}/*H_2O system (from 2 to 4 ps).

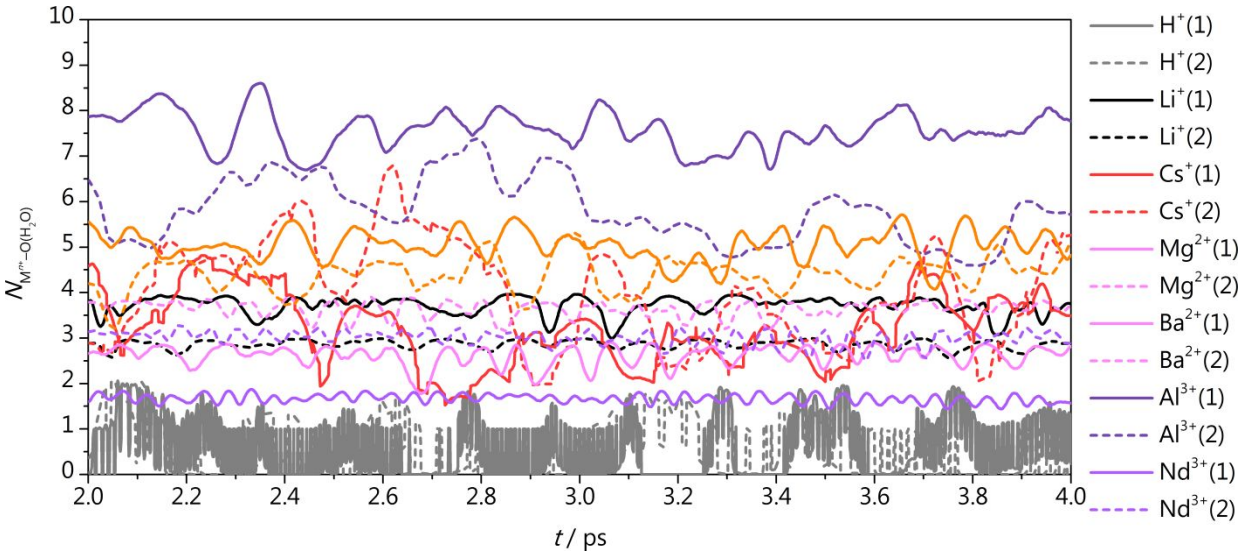

Figure S17. Cation coordination numbers to oxygen atoms in solvent molecules ($N_{M\text{-}O(H2O)}$) for the Au/water/M^{n+}/*H_2O system (from 2 to 4 ps).

Supporting Table 4. Cation coordination numbers to oxygen atoms in adsorbed H_2O ($N_{M\text{-}O(H2O)}$) as calculated through Supporting Equation 4 for Au/water/M^{n+}/H_2O during 2 ps AIMD at 300 K (Figures S16-S17). Coordination numbers are reported as averages with their associated standard deviation $\sigma(N_{cat\text{-}O})$, median, maximum, and minimum values.

	$N_{M\text{-}O(H2O)}$ (Au/water/M^{n+}/*H_2O)				$N_{M\text{-}O(CO2)}$ (Au/water/M^{n+}/*H_2O)			
M^{n+}	Mean	Median	Max	Min	Mean	Median	Max	Min
H^+	0.6 ± 0.6	0.2	2.1	0.0	0.0 ± 0.0	0.0	0.0	0.0
Li+	2.87 ± 0.09	2.9	3.0	2.6	0.0 ± 0.0	0.0	0.0	0.0
Cs^+	4.0 ± 1.1	4.0	6.8	2.0	0.5 ± 0.4	0.6	1.0	0.0
Mg^{2+}	2.6 ± 0.2	2.7	2.9	1.8	0.0 ± 0.0	0.0	0.0	0.0
Ba^{2+}	5.8 ± 0.7	5.8	7.4	4.6	0.6 ± 0.5	0.9	1.0	0.0
Al^{3+}	1.67 ± 0.09	1.7	1.9	1.4	0.7 ± 0.1	0.7	0.8	0.4
Nd^{3+}	4.4 ± 0.4	4.4	5.3	3.2	0.0 ± 0.2	0	1.0	0

Determination of the activation barriers.

To estimate the activation energies for H_2O and H_3O^+ dissociation and CO_2 protonation, we considered an Au/2-3H_2O/M^{n+}/*ads* system, with simplified cation solvation shell with 2-3 water molecules. Supporting Equations 10-12 define the processes for 3 water molecules in the solvation shell. We then removed $n-1$ protons (n for H_3O^+ dissociation) from the system to keep an extra electron in the system (n = 1, 2, 3 for proton and alkali, bivalent and trivalent cations respectively). Then, we let *CO_2, *COOH, *H_3O^+, *H_2O, H_2O + *H and OH^- + *H adsorb close to the cation, and we further optimized the overall system Au/2-3H_2O/M^{n+}/*ads* (*ads* = *CO_2, *COOH, *H_3O^+, *H_2O, H_2O + *H and OH^- + *H). Activation energies were calculated trough the Nudged Elastic Band (NEB) method and all of them exhibit a single imaginary vibrational frequency.[29] Gibbs free energies were calculated at 298.15 K by correcting DFT energies for entropic contributions. The energy references were chosen as CO_2(g), H_2(g) and H_2O(g) and single point calculations for the Au/2-3H_2O/M^{n+} system.

$$* CO_2^- \cdots M^{n+}(H_2O)_{(3-n)} + (n-1)OH^- \rightleftharpoons * COOH + M^{n+}(H_2O)_{(3-n-1)} + nOH^- \quad (10)$$

$$* H_2O + e^- + M^{n+}(H_2O)_{(3-n)} + (n-1)OH^- \rightleftharpoons * H + OH^- \cdots M^{n+}(H_2O)_{(3-n)} + (n-1)OH^- \quad (11)$$

$$* H_3O^+ + e^- + M^{n+}(H_2O)_{(3-n)} + nOH^- \rightleftharpoons * H + H_2O \cdots M^{n+}(H_2O)_{(3-n)} + nOH^- \quad (12)$$

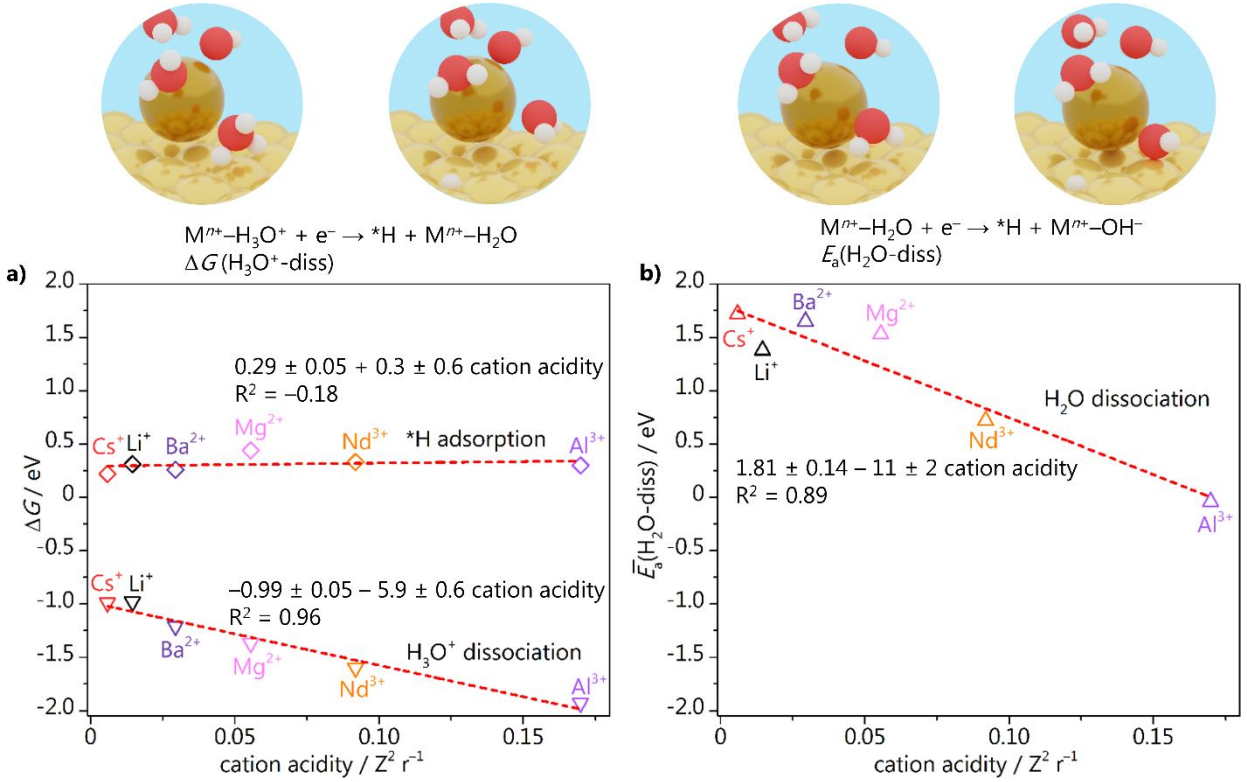

Figure S18. a) Gibbs free energy for *H adsorption (diamonds) and H_3O^+ dissociation (down-pointing triangles, Supporting Equation 12) vs. cation acidity, calculated with 3 H_2O molecules in cation solvation shell. b) Activation barrier for water dissociation (up-pointing triangles, Supporting Equation 11) vs. cation acidity, calculated as average of the calculated values for 2 and 3 H_2O molecules in cation solvation shell. In the insets, Au, Cs, H, and O atoms are portrayed as yellow, dark yellow, white, and oxygen spheres, respectively.

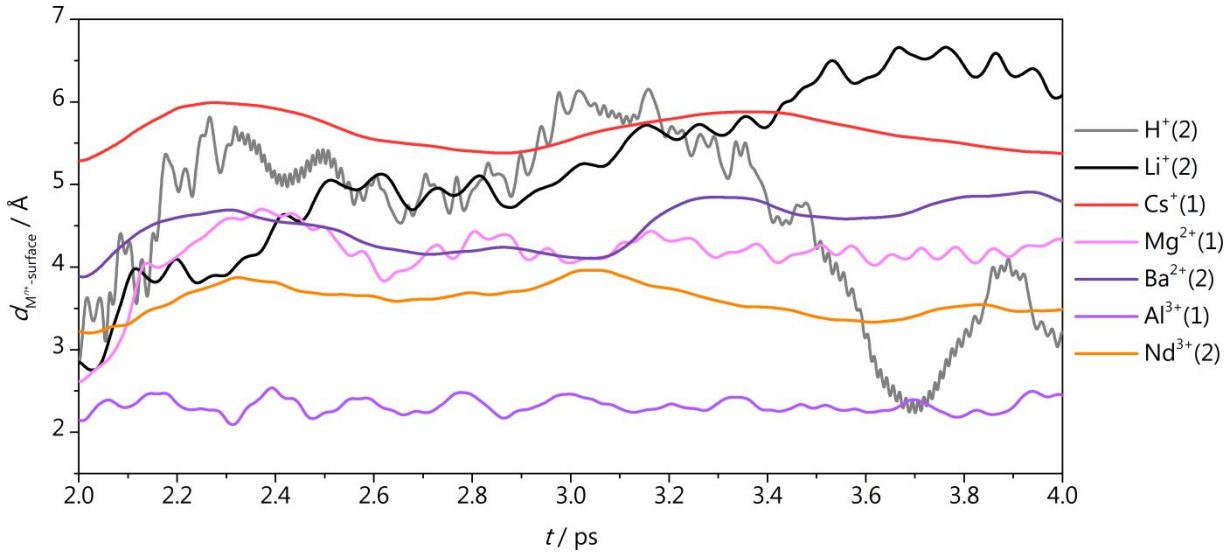

Figure S19. Distance between multivalent cation (M^{n+}) and surface calculated for the Au/water/M^{n+}/*CO_2 system (from 2 to 4 ps).

Supporting Table 5. Cation coordination numbers to oxygen atoms in solvent molecules ($N_{M\text{-}O(H2O)}$) and adsorbed CO_2 ($N_{M\text{-}O(CO2)}$) as calculated through Supporting Equation 3 for Au/water/M^{n+}/*CO_2 during 2 ps AIMD at 300 K (Figures S16-S17). Coordination numbers are reported as averages with their associated standard deviation $\sigma(N_{M\text{-}O})$, median, maximum, and minimum values.

	$N_{M\text{-}O(H2O)}$ (Au/water/M^{n+}/*CO_2)				$N_{M\text{-}O(H2O)}$ (Au/water/M^{n+}/*CO_2)			
M^{n+}	Mean	Median	Max	Min	Mean	Median	Max	Min
H^+	0.5 ± 0.6	0.1	1.9	0.0	0 ± 3E–4	0.0	0.01	0.0
Li+	3.1 ± 0.5	3.0	3.9	2.0	0.0 ± 0.2	0.0	1.0	0.0
Cs^+	3.5 ± 0.6	3.5	4.8	2.0	0.7 ± 0.4	0.8	1.8	0.0
Mg^{2+}	3.0 ± 0.4	3.0	3.8	2.0	0.6 ± 0.4	0.7	1.0	0.0
Ba^{2+}	5.6 ± 0.7	5.5	7.1	3.8	0.9 ± 0.2	1.0	1.0	0.1
Al^{3+}	1.63 ± 0.12	1.6	1.9	1.2	0.5 ± 0.2	0.5	0.9	0.0
Nd^{3+}	3.9 ± 0.4	3.9	4.7	2.8	0.9 ± 0.2	0.9	1.0	0

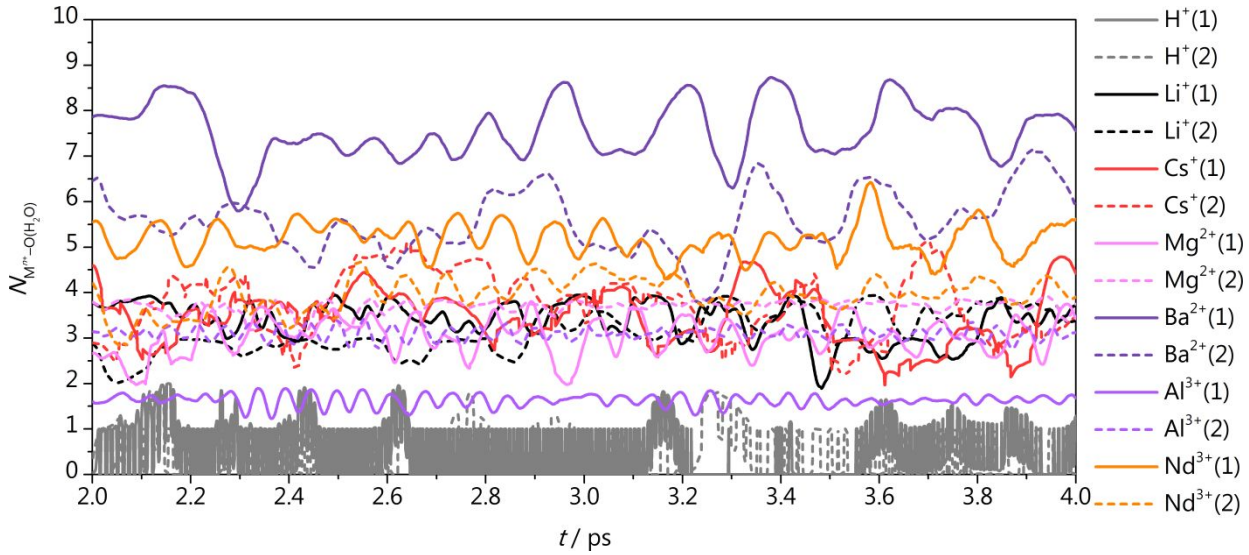

Figure S20. Cation coordination numbers to oxygen atoms in solvent molecules ($N_{M\text{-}O(H2O)}$) for the Au/water/M^{n+}/*CO_2 system (from 2 to 4 ps).

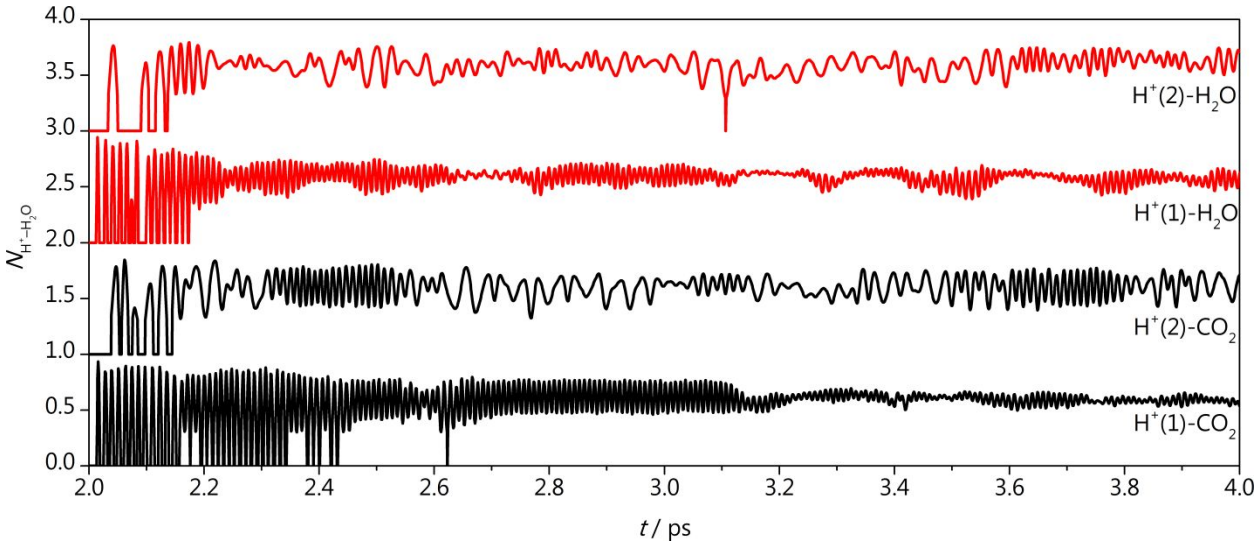

Figure S21. Bond formation between H^+ and neighboring water molecule for Au/water/H^+/*CO_2 system and Au/water/H^+/*H_2O system (from 2 to 4 ps). Proton is not effective as a CO_2 reduction promoter, since it combined with a neighboring water molecule to form a H_3O^+ after less than 0.2 ps.

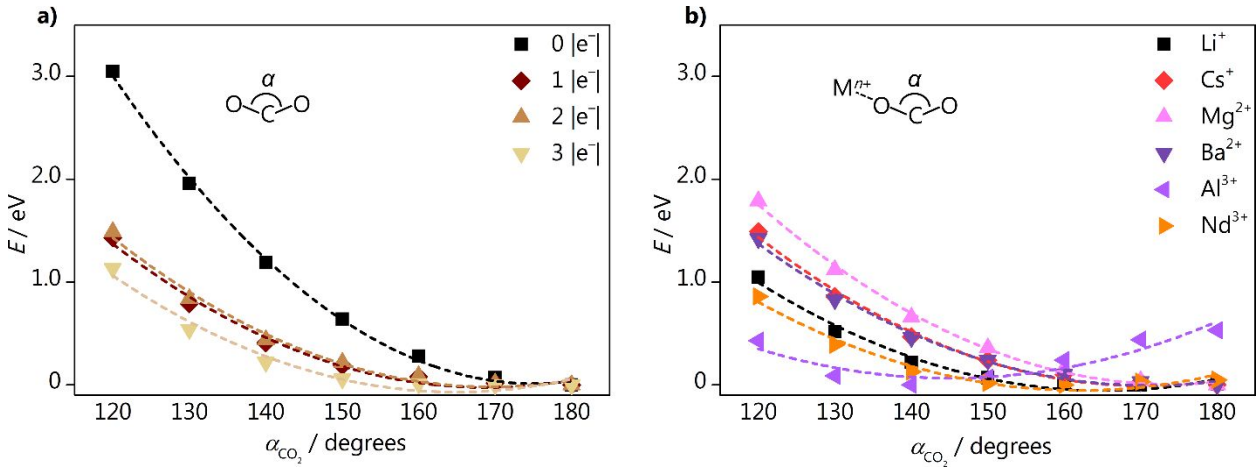

Figure S22. DFT energy of a free CO_2 a) and b) a CO_2 coordinated to a multivalent cation as a function of the CO_2 activation angle, α. Lower α values indicate CO_2 activation. $M^{n+}\cdots O(CO_2)$ distances have been set according to AIMD results (Table S1). Different colors and shapes highlight a), additional electrons in the simulation cell (from 1 to 3) and b), different cation species. Dashed lines represent a quadratic fit over the data points.

Supporting Table 6. Fit parameters for quadratic correlations shown in Figure S21: $E = \mathrm{a} + \mathrm{b} * \alpha_{CO_2} + \mathrm{c} * \alpha_{CO_2}{}^2$

System	a / eV	b / eV degrees^{-1}	c / eV degrees^{-2}	R^2
CO_2 (0 |e⁻|)	+30 ± 1	–0.35 ± 0.02	+9.9E-04 ± 6E-05	0.998
CO_2 (1 |e⁻|)	+17 ± 2	–0.20 ± 0.02	+5.9E-04 ± 7E-05	0.98
CO_2 (2 |e⁻|)	+17 ± 2	–0.20 ± 0.02	+5.9E-04 ± 7E-05	0.985
CO_2 (3 |e⁻|)	+15 ± 2	–0.19 ± 0.03	+5.6E-04 ± 9E-05	0.97
$Li^+\cdots CO_2$ (1 |e⁻|)	+14 ± 2	–0.17 ± 0.02	+5.2E-04 ± 7E-05	0.97
$Cs^+\cdots CO_2$ (1 |e⁻|)	+17 ± 1	–0.19 ± 0.02	+5.7E-04 ± 7E-05	0.988
$Mg^{2+}\cdots CO_2$ (2 |e⁻|)	+18 ± 1	–0.209 ± 0.014	+6.0E-04 ± 5E-05	0.996
$Ba^{2+}\cdots CO_2$ (2 |e⁻|)	+16 ± 1	–0.18 ± 0.02±	+5.3E-04 ± 6E-05	0.989
$Al^{3+}\cdots CO_2$ (3 |e⁻|)	+10 ± 2	–0.13 ± 0.03	+4.52E-04 ± 1.1E-04	0.77
$Nd^{3+}\cdots CO_2$ (3 |e⁻|)	+13 ±2	–0.16 ± 0.02	+4.9E-04 ± 7E-05	0.96

References

(1) Monteiro, M. C. O.; Jacobse, L.; Koper, M. T. M. Understanding the Voltammetry of Bulk CO Electrooxidation in Neutral Media through Combined SECM Measurements. *J. Phys. Chem. Lett.* **2020**, *11* (22), 9708–9713.

(2) Lide, D. R. *CRC Handbook of Chemistry and Physics*, 84th ed.; Lide, D. R., Ed.; CRC Press, 2003; Vol. 85.

(3) Kresse, G.; Furthmüller, J. Efficient Iterative Schemes for Ab Initio Total-Energy Calculations Using a Plane-Wave Basis Set. *Phys. Rev. B* **1996**, *54*, 11169–11186.

(4) Kresse, G.; Furthmüller, J. Efficiency of Ab-Initio Total Energy Calculations for Metals and Semiconductors Using a Plane-Wave Basis Set. *Comput. Mater. Sci.* **1996**, *6*, 15–50.

(5) Perdew, J. P.; Burke, K.; Ernzerhof, M. Generalized Gradient Approximation Made Simple. *Phys. Rev. Lett.* **1996**, *77*, 3865–3868.

(6) Grimme, S. Semiempirical GGA-Type Density Functional Constructed with a Long-Range Dispersion Correction. *J. Comput. Chem.* **2006**, *27*, 1787–1799.

(7) Bucko, T.; Hafner, J.; Lebègue, S.; Ángyán, J. G. Improved Description of the Structure of Molecular and Layered Crystals: Ab Initio DFT Calculations with van Der Waals Corrections. *J. Phys. Chem. A* **2010**, *114*, 11814–11824.

(8) Almora-Barrios, N.; Carchini, G.; Błoński, P.; López, N. Costless Derivation of Dispersion Coefficients for Metal Surfaces. *J. Chem. Theory Comput.* **2014**, *10*, 5002–5009.

(9) Blöchl, P. E. Projector Augmented-Wave Method. *Phys. Rev. B* **1994**, *50*, 17953–17979.

(10) Kresse, G.; Joubert, D. From Ultrasoft Pseudopotentials to the Projector Augmented-Wave Method. *Phys. Rev. B* **1999**, *59*, 1758–1775.

(11) Dudarev, S. L.; Botton, G. A.; Savrasov, S. Y.; Humphreys, C. J.; Sutton, A. P. Electron-Energy-Loss Spectra and the Structural Stability of Nickel Oxide: An LSDA+U Study. *Phys. Rev. B* **1998**, *57* (3), 1505–1509.

(12) Kozub, A. L.; Shick, A. B.; Máca, F.; Kolorenč, J.; Lichtenstein, A. I. Electronic Structure and Magnetism of Samarium and Neodymium Adatoms on Free-Standing Graphene. *Phys. Rev. B* **2016**, *94* (12), 125113.

(13) Monteiro, M. C. O.; Dattila, F.; Hagedoorn, B.; García-Muelas, R.; López, N.; Koper, M. T. M. Absence of CO2 Electroreduction on Copper, Gold and Silver Electrodes without Metal Cations in Solution. *Nat. Catal.* **2021**, *4* (8), 654–662.

(14) Bellarosa, L.; García-Muelas, R.; Revilla-López, G.; López, N. Diversity at the Water–Metal Interface: Metal, Water Thickness, and Confinement Effects. *ACS Cent. Sci.* **2016**, *2* (2), 109–116.

(15) Marx, D.; Hutter, J. *Ab Initio Molecular Dynamics: Basic Theory and Advanced Methods*; Cambridge University Press, 2009.

(16) Nosé, S. A Unified Formulation of the Constant Temperature Molecular Dynamics Methods. *J. Chem. Phys.* **1984**, *81*, 511–519.

(17) Hoover, W. G. Canonical Dynamics: Equilibrium Phase-Space Distributions. *Phys. Rev. A* **1985**, *31*,

1695–1697.

(18) Feibelman, P. J. Surface-Diffusion Mechanism versus Electric Field: Pt/Pt(001). *Phys. Rev. B* **2001**, *64* (12), 125403.

(19) McCrum, I. T.; Bondue, C. J.; Koper, M. T. M. Hydrogen-Induced Step-Edge Roughening of Platinum Electrode Surfaces. *J. Phys. Chem. Lett.* **2019**, *10* (21), 6842–6849.

(20) Chen, L. D.; Urushihara, M.; Chan, K.; Nørskov, J. K. Electric Field Effects in Electrochemical CO_2 Reduction. *ACS Catal.* **2016**, *6* (10), 7133–7139.

(21) White, R. E.; Bockris, J. O.; Conway, B. E. *Modern Aspects of Electrochemistry*; Kluwer Academic Publishers, 2002.

(22) Makov, G.; Payne, M. Periodic Boundary Conditions in Ab Initio Calculations. *Phys. Rev. B* **1995**, *51*, 4014–4022.

(23) Waegele, M. M.; Gunathunge, C. M.; Li, J.; Li, X. How Cations Affect the Electric Double Layer and the Rates and Selectivity of Electrocatalytic Processes. *J. Chem. Phys.* **2019**, *151* (16), 160902.

(24) Marcus, Y. Ionic Radii in Aqueous Solutions. *Chem. Rev.* **1988**, *88* (8), 1475–1498.

(25) Dattila, F.; García-Muelas, R.; López, N. Active and Selective Ensembles in Oxide-Derived Copper Catalysts for CO_2 Reduction. *ACS Energy Lett.* **2020**, *5*, 3176–3184.

(26) Resasco, J.; Chen, L. D.; Clark, E.; Tsai, C.; Hahn, C.; Jaramillo, T. F.; Chan, K.; Bell, A. T. Promoter Effects of Alkali Metal Cations on the Electrochemical Reduction of Carbon Dioxide. *J. Am. Chem. Soc.* **2017**, *139* (32), 11277–11287.

(27) Nørskov, J. K.; Rossmeisl, J.; Logadottir, A.; Lindqvist, L.; Kitchin, J. R.; Bligaard, T.; Jónsson, H. Origin of the Overpotential for Oxygen Reduction at a Fuel-Cell Cathode. *J. Phys. Chem. B* **2004**, *108* (46), 17886–17892.

(28) Haynes, W. M. *Handbook of Chemistry and Physics*, 95th ed.; CRC Press: New York, 2014.

(29) Henkelman, G.; Jónsson, H. Improved Tangent Estimate in the Nudged Elastic Band Method for Finding Minimum Energy Paths and Saddle Points. *J. Chem. Phys.* **2000**, *113* (22), 9978–9985.